Vertical Takeoff and Landing of Flexible Wing Kite Power Systems

Rapp, Sebastian; Schmehl, Roland

DOI
10.2514/1.G003535

Publication date
2018

Document Version
Final published version

Published in
Journal of Guidance, Control, and Dynamics: devoted to the technology of dynamics and control

JOURNAL OF GUIDANCE, CONTROL, AND DYNAMICS
Vol. 41, No. 11, November 2018

Vertical Takeoff and Landing of Flexible Wing Kite Power Systems

Sebastian Rapp* and Roland Schmehl†
Delft University of Technology, 2629 HS Delft, The Netherlands

DOI: 10.2514/1.G003535

In this work, a novel vertical takeoff and landing methodology for flexible wing kite power systems is presented. Starting from a basic mast-based launching and landing concept, the operational envelope will be enlarged using the external assistance of a multicopter. The multicopter is used to drag the kite along a specified launching path until the operational altitude is reached, where the kite is detached and steered to its characteristic parking position while the multicopter lands. The landing of the kite will be conducted without multicopter assistance, and solely the winch will be used to pull the kite toward the ground station. For all maneuvers, flight control algorithms are presented, and the feasibility of the proposed methodology is analyzed using a developed simulation environment incorporating models for the kite, multicopter, ground station, and the tethers that connect the individual subsystems.

I. Introduction

ONE of the open technical challenges of airborne wind energy is the automation of the launching and landing procedures for flexible as well as rigid wing kite power systems [1,2,3]. To ensure the commercial viability of the technology, these procedures, which envelope the operational phase of the system, have to be highly reliable and robust in different weather conditions. However, as an atmospheric phenomenon, wind is fluctuating in magnitude and direction, on short and long time scales, which makes launching and landing in particular challenging. For most of the practically pursued system concepts, the launching starts from a configuration at which the tether is short and the airborne device is consequently close to the ground station. This requires either external supporting devices for the launching and the landing phase such as catapults for a translational launch, a rotating arm mechanism for a rotational launch, or additional onboard engines. In practice, several companies that operate rigid wing kite power systems such as e-kite, Kitemill, Makani, and TwingTec are in favor of additional onboard engines that enable a vertical takeoff and landing (VTOL) solution [4]. One advantage over other launching and landing concepts is that the required additional infrastructure for a VTOL system is negligibly small and comparably simple because no additional mast, rotating platform, or rotating arm is required. This makes the VTOL approach a cheaper and more mobile solution compared to other concepts. Furthermore, the kite system can be launched in an arbitrary direction, which is not possible if, for instance, a horizontal takeoff approach is chosen, unless the corresponding launching platform can be rotated, which of course increases the complexity and cost. Moreover, precise landing maneuvers are possible because the wing can be pulled toward the ground station while the rotor thrusts can be used to stabilize the kite attitude in a quasi-hover state. For a more detailed comparison of different launching and landing approaches for rigid wing kite power systems, the reader is referred to [2].

Companies and institutes with flexible wing systems have tested different strategies including a simple static mast-based launch and landing (which is used by the company SkySails), an upside-down swing-up launching as presented in [3], or a launching and landing system based on a rotating arm (a concept pursued by the company KiteGen [4]). The major disadvantage of these concepts is their strong dependency on the wind conditions in ground proximity, resulting in a limited control authority at low wind speeds. Because of the wind shear effect, the wind velocities at ground level are generally low and the turbulence level is high, with both conditions negatively affecting the robustness and reliability of these launching and landing mechanisms.

In general, a VTOL approach for flexible kites leads to additional technical challenges because the rotors are difficult to integrate into the wing. One possibility is presented in [5], where the rotors are instead mounted on the steering unit, and the kite is dragged upside down to the operational altitude. The downside of this approach is the required onboard power that is necessary to compensate kite weight as well as the aerodynamic forces. Moreover, the additional mass has to be carried onboard during the entire power cycle, which has a negative impact on the overall system performance. Furthermore, scaleability issues could arise for larger kites that generate large aerodynamic forces that might be difficult to compensate by the onboard power of the multicopter system.

Besides the work in [5], the potential of VTOL for flexible kite power systems has not yet been addressed in the scientific community. The present work tries to fill this gap by proposing a hybrid VTOL approach. It complements the simplicity of a static mast-based approach, whose operational envelope will be extended with an externally attached multicopter system. In fact, it drags the kite to the operational altitude only in certain wind conditions that would not allow a passive mast-based launch. In case of a sufficiently high ground wind speed, the kite will be launched without the external assistance of the multicopter. Both concepts, mast and multicopter launching, can be regarded as complementary because the static mast-based launching is appealing due to its simplicity and autonomy with the disadvantage that it works only well in combination with a sufficiently high ground wind speed, whereas the VTOL concept works most reliably in low-wind conditions at the cost of increased complexity. Compared to the approach presented in [5], the present concept will suffer less from the scaleability problem because the higher aerodynamic forces generated by larger kites can be exploited explicitly during the launching, and the additional mass of the VTOL system will not deteriorate the overall power output.

The presented approach in this paper allows, in theory, to launch multiple kite systems in a kite park with a single multicopter. However, such a fully automated launching procedure is challenging due to the required automation of the attachment process, as already pointed out in [5]. In the present work, the requirement for full autonomy will be weakened, such that a manual attachment of the multicopter still complies with the system requirements. Nonetheless, the presented approach can be regarded as a preliminary study of a single-kite VTOL concept that can be extended to a multiple-kite VTOL concept in the future. This would require the development of the attachment automation, which is out of the scope of this paper, but leaves ample space for future research.

Photographic footage of a preliminary small-scale experimental study conducted in cooperation with Kitepower B.V. is shown in Fig. 1, and a schematic visualization is depicted in Fig. 2.

Received 23 December 2017; revision received 29 April 2018; accepted for publication 30 April 2018; published online 24 July 2018.

*Ph.D. Researcher, Faculty of Aerospace Engineering, Kluyverweg 1; s.rapp@tudelft.nl.

†Associate Professor, Faculty of Aerospace Engineering, Kluyverweg 1; r.schmehl@tudelft.nl.

Fig. 1 Custom-made drone launching a 9 m^2 kite. Photo credit: Marcos Jerez Venegas.

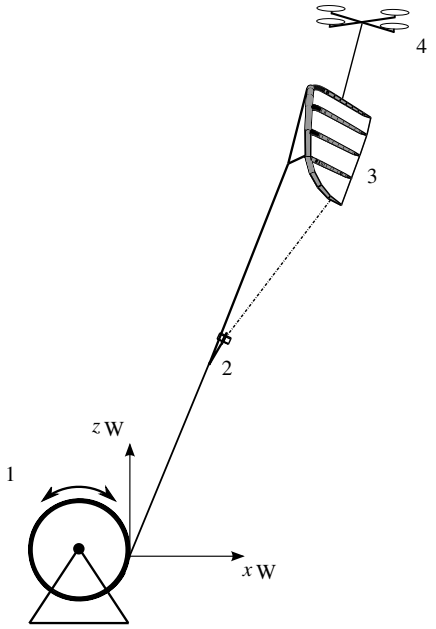

Fig. 2 Sketch of drone assisted launching with ground station 1, kite steering unit 2, kite 3, and multicopter 4.

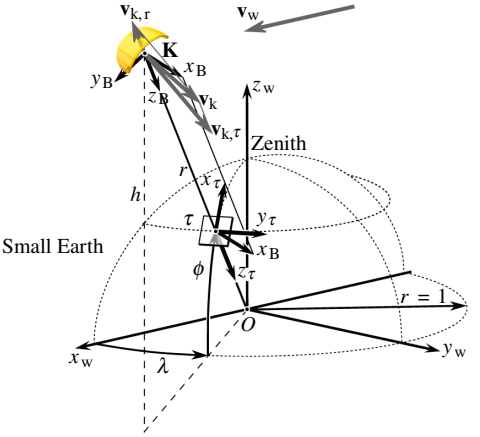

Fig. 3 Visualization of wind frame *W*, body-fixed frame *B*, and tangential plane frame *τ*.

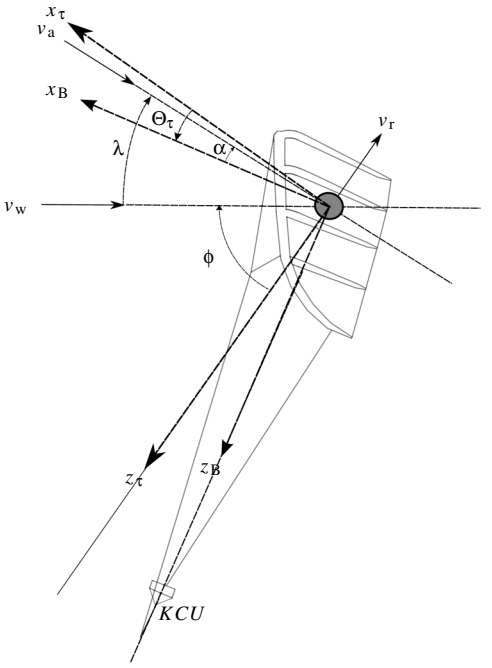

Fig. 4 Visualization of the launching kinematics.

The paper is structured as follows. In Sec. II, a detailed theoretical analysis is conducted with the aim to develop boundary conditions for the launching and landing phase. In Sec. III, simulation models for all the involved subsystems are developed. For each of the subsystems, a controller is designed in Sec. IV. Simulation results will be presented in Sec. V along with an overview of the developed methodology, and a conclusion is given in Sec. VI.

II. Theoretical Analysis

A. Boundaries of Assisted and Nonassisted Launching and Landing Maneuvers

The subsequent calculations require the definitions of several coordinate systems. The wind frame W will be used to define the position of the kite and is defined as shown in Fig. 3, where the x_W axis is pointing in downwind direction and the z_W axis is pointing upward, while the y_W axis forms a right-hand coordinate system together with x_W and z_W. The tangential plane frame τ will be used in combination with a body-fixed frame B to describe the orientation of the kite. Figure 4 shows the definitions of the τ as well as the B frame, whose origins are both attached to the center of gravity of the kite. The z_τ axis is pointing toward the origin of the wind frame W, and the x_τ axis points toward the zenith position, which is located above the ground station. Note that the τ frame is defined equivalently to the north–east–down frame for a small Earth with radius of 1 and center at the origin of the W frame, which is visualized in Fig. 3. The body-fixed x_B axis is parallel to the center chord of the wing, whereas the z_B axis points from the center of gravity of the kite toward the steering unit.

For the subsequent analysis, it is assumed that the steering unit coincides with the center of gravity of the kite. This point-mass assumption of the kite system will be dropped in Sec. III, where six-degree-of-freedom simulation models are developed. It turns out that the point-mass assumption in this section leads to conservative results, which can be improved by defining a pitch angle Θ_τ about which the wing is rotated relatively to the tangential plane frame. In reality, this rotation is mainly caused by the drag as well as the weight of the tether and the steering unit, which lowers the angle of attack of the kite.

In the present work, boundaries for the launching and landing procedures are defined in terms of equilibrium positions that a kite is able to reach if the wind speed is high enough to keep the kite airborne. For a kite that is not flying crosswind, this equilibrium position is located in the downwind direction at a certain elevation angle $\phi = \phi_{\text{eq}}$ and results from a moment equilibrium around the tether attachment point on the ground. The equilibrium is often denoted as the parking position in the airborne wind energy literature [6]. Most publications regarding flight control of kites assume that the kite is already airborne, and the existing control approaches

usually start controlling the kite from the parking position into crosswind flight and back. The work in this paper aims to fill this gap by providing a methodology and a simulation environment that allows to guide the kite from the ground to the parking position and from the parking position back to the ground. Because of the modularity, the presented approach can be combined later on with existing crosswind flight controllers such as the control approach presented in a previous work of the author [7]. The goal of the kite launching maneuver will be to control the kite from the ground to the parking position with or without assistance of the multicopter depending on the wind conditions. Based on an equilibrium analysis, a minimum wind speed in ground proximity can be used as a threshold that, if not reached, will require the assistance of the multicopter system to launch the kite to higher altitudes with sufficiently high wind speed. All feasible parking positions are primarily a function of the wind speed. The contributing forces that are used to derive the equilibrium condition are the aerodynamic force consisting of drag D and lift L as well as the weight $m_k g$ of the kite. The tether force is neglected in the moment equilibrium due to the straight tether assumption. This leads to the well-known equation for the parking elevation angle:

$$\tan(\phi) - \frac{L(\phi) - m_k g}{D(\phi)} \stackrel{!}{=} 0 \tag{1}$$

with

$$L = 0.5\rho S_k C_L(\alpha) v_a^2 \tag{2}$$

$$D = 0.5\rho S_k C_D(\alpha) v_a^2 \tag{3}$$

and

$$\alpha = \frac{\pi}{2} - \lambda - \phi + \Theta_\tau \tag{4}$$

where Θ_τ is the pitch angle of the kite with respect to the tangential plane, ρ is the air density, S_k is the kite reference area, and v_a is the absolute value of the apparent wind speed vector as defined in Eq. (6). λ is defined as the angle between the wind speed vector and the apparent wind speed (see Fig. 4) and is defined by the difference of the wind and the kinematic kite speed:

$$\lambda = \arccos\left(\frac{\boldsymbol{v}_a^T \boldsymbol{v}_w}{\|\boldsymbol{v}_a\|_2 \|\boldsymbol{v}_w\|_2}\right) \tag{5}$$

where the apparent wind speed vector $\boldsymbol{v}_a$ is given by

$$\boldsymbol{v}_a = \boldsymbol{v}_w - \boldsymbol{v}_k \tag{6}$$

In the following, the absolute values for $\boldsymbol{v}_a$, $\boldsymbol{v}_w$, and $\boldsymbol{v}_k$ are denoted with v_a, v_w, and v_k. Note that, in case of a stationary kite, $v_k = 0$ and hence $\lambda = 0$. For $C_L(\alpha)$ and $C_D(\alpha)$, the same values as in [6] are used because they reflect the aerodynamic properties of the kite used in the present work. Equation (1) depends implicitly on ϕ; hence, it has to be solved numerically. The solutions of Eq. (1) are calculated for different wind speeds and pitch angles Θ_τ and visualized in the contour plot of Fig. 5, where the contour lines represent the parking elevation angles ϕ. Note that, to ensure a minimum distance to the ground, an additional constraint in the form of a minimum elevation angle of approximately 45 deg is imposed. Furthermore, in practice, positive pitch angles are not obtained; hence, the mathematical solutions for $\Theta_\tau \geq 0$ deg can be ignored. It can be observed that, depending on the kite pitch angle Θ_τ, the boundary for the minimal wind speed changes and usually ranges from ≈ -5.4 m/s with $\Theta_\tau = -20$ deg to ≈ -8 m/s with $\Theta_\tau = 0$ deg.

For the subsequent launching and landing analysis, it is beneficial to look at equilibrium points with a constant radial velocity v_r, which in the case of a straight tether is equal to the reeling-out velocity. This

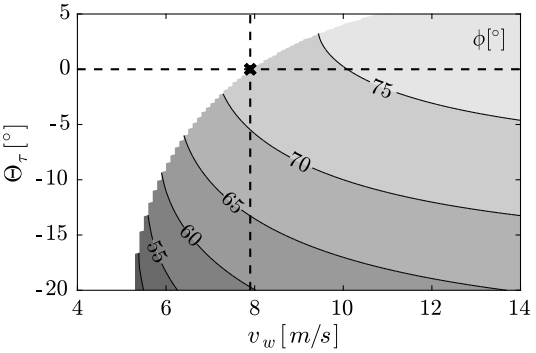

Fig. 5 Parking elevation angle ϕ as a function of pitch angle Θ_τ and wind speed v_w.

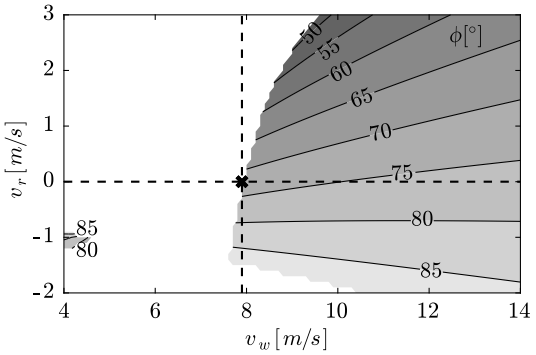

Fig. 6 Parking elevation angle ϕ as a function of v_r and v_w with fixed $\Theta_\tau = 0$ deg.

enables to calculate boundaries that frame the nonassisted launching envelope as a function of v_r. Solving Eq. (1) numerically for different wind and reeling-out speeds yields the results as depicted in the contour plot of Fig. 6. Note the consistency of the solutions in Figs. 5 and 6 for the parking equilibrium elevation angle with $v_r = 0$ m/s and $\Theta_\tau = 0$ deg.

As mentioned previously, assuming a zero pitch angle of the kite for the calculation of the equilibrium points induces conservatism, which will be discussed in the following. Based on the results in Fig. 6, it can be observed that a kite attached to a vertical mast (i.e., $\phi = 90$ deg) is not within the depicted feasible solution space. If for instance the kite is launched with $v_r = 0.5$ m/s, a wind speed of $v_w \leq 8.1$ m/s and additionally an initial inclination $\phi = 67$ deg are required; otherwise, no launching along equilibrium points is possible. For arbitrary reeling-out velocities $v_r > 0$, the wind speed and elevation angles have to satisfy $v_w > 8$ m/s and $\phi < 72$ deg, respectively, to enable a nonassisted launching. This restriction of course does not hold for the multicopter-assisted launch because the force differential required to lift the kite is provided by the multicopter thrust.

In theory, the reeling-out velocity determines the required initial inclination of the kite for a given wind speed. The choice for the reeling-out velocity for a given wind speed is a design parameter and could be determined based on the to-be-expected parking elevation angle. As can be observed in Fig. 6, decreasing the reeling-out velocity for a given wind speed will increase the equilibrium elevation angle. For instance, assuming that just before the target altitude a wind speed of $v_w = 11$ m/s is present and assuming that the kite is launched with a constant radial velocity controlled by the winch (e.g., $v_r = 1$ m/s), then stopping reeling out (i.e., $v_r \to 0$) creates a velocity component perpendicular to the radial velocity v_r (i.e., in x_τ the direction) because the equilibrium elevation angle increases up to approximately 76 deg. This observation will be used later on for the path planning.

From the results depicted in Fig. 5, it can be observed that, for $\Theta_\tau \in (-7.5, 0$ deg), which is the usual range of the pitch angle observed

during experiments, and wind speeds $v_w > 8$ m/s, which is required for nonassisted kite launches, the parking elevation angle will be greater than 64 deg, whereas the maximum elevation angle will be around 73 deg for $v_{w,\max} = 14$ m/s. This means that launching path elevation angles up to 73 deg are possible because it is desired that the kite will move in the positive x_τ direction if $v_r \to 0$. Note that the equilibrium path angle during the launching will always be smaller than the parking elevation angle. Eventually, the maximum reeling-out speed is theoretically determined by an operational constraint regarding the minimum possible elevation angle during launching provided for instance by an inclined mast. In addition, higher reeling-out speeds require higher wind speeds to compensate the loss in apparent wind speed. The smallest reeling-out speed is essentially limited by other operational constraints such as requirements on the launching time or the accuracy of the winch controller at low rotational winch speeds. It is assumed that, in practice, the reeling-out speed will be between 0.5 and 1.0 m/s. To illustrate the effect of the pitch angle on the equilibrium elevation angles as function of wind speed and reeling-out speed, the results for $\Theta_\tau = -7.5$ deg are depicted in Fig. 7. By comparing Fig. 6 with the results depicted in Fig. 7, it can be observed that the pitching down of the kite leads to smaller lower bounds on the minimal wind speed, which reflects the mentioned conservatism. This indicates that, for a nonconservative estimation of equilibrium points, the pitch angle of the kite plays a major role. Because the pitch of the kite is mainly influenced by the tether drag and steering unit weight, the simple point-mass model is not sufficient to calculate the optimal bounds, but because of the conservatism, it leads to safe bounds, which is sufficient for the further analysis in the present work.

An equivalent analysis can be made regarding a steady landing. Steady solutions with $v_r \leq 0$ are depicted in Fig. 6. The results in Fig. 6 and Fig. 7 indicate that, also during the reeling-in phase, negative pitch angles shift the minimal wind speeds required for a steady descent to lower values. Therefore, depending on the wind measurement on the ground, conservative reeling-in speeds that lead to a steady descent of the kite can be selected. Note that, if a reeling-in speed higher than the recommended speed based on the results in Fig. 6 is chosen, the kite can overshoot the ground station (i.e., $\phi > 90$ deg), which is not desirable from an operational point of view.

B. Multicopter Performance Definition

In this section, the required power and resulting mass of the multicopter will be estimated based on the flight time as well as the mass of the kite and tether. According to [5], the required power $P_{t,e}$ to lift a certain mass with a multicopter system can be estimated based on momentum theory. $P_{t,e}$ essentially depends on efficiency factor η_e, launching time t_L, battery energy density γ_E, mass for electronics and airframe (m_0), kite mass including steering unit mass (m_k), maximum tether mass m_t, power-to-mass ratio λ_M, gravity g, air density ρ, thrust-to-weight ratio λ, and total swept rotor area A_p. Following the steps in [5], an implicit expression for $P_{t,e}$ can be derived, which is given by

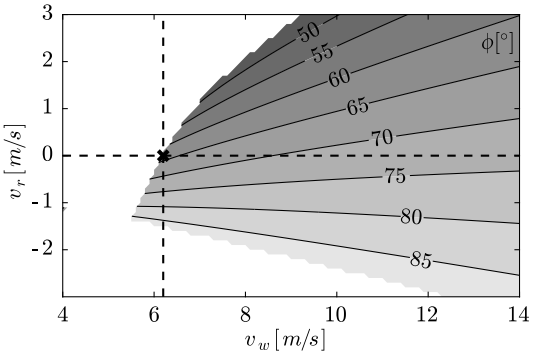

Fig. 7 Parking elevation angle ϕ as a function of v_r and v_w with fixed $\Theta_\tau = -7.5$ deg.

Table 1 Design parameters

Parameter	Value
γ_E	130 W · h/kg
m_k	14.61 kg
m_t	1.3 kg
A_p	0.28^2
λ_m	0.2 kg/kW
m_0	0.5 kg
ρ	1.225 kg/m^3
λ	1.5
g	9.81 m/s^2
η_e	0.8
t_L	3 min

$$P_{t,e} = \frac{1}{\eta_e}\sqrt{\frac{(((P_{t,e}t_L/\gamma_E) + m_0 + m_k + m_t + P_{t,e}\lambda_M)g\lambda)^3}{2\rho A_p}} \tag{7}$$

This expression can be solved numerically for $P_{\text{tot},e}$. The resulting battery mass m_b is then given by

$$m_b = \frac{P_{t,e}t_L}{\gamma_E} \tag{8}$$

The chosen numerical values in this work are summarized in Table 1, selected mainly based on the values proposed in [5,6]. A mean launching time t_L of 3 min has been chosen in this work, which in combination with a mean launching velocity of 1 m/s produced reasonable results. In general, if there is no requirement for the maximum launching time, smaller launching velocities are preferable to save power and to reduce the aerodynamic effects acting on the multicopter. The thrust to weight ratio $\lambda = 1.5$ seems to be reasonable because no highly dynamic flight paths will be flown. Moreover, the kite will compensate at least partially its own weight by exploiting the generated lift force. Solving Eq. (7) with the values in Table 1 yields a required power of $P_{t,e} \approx 11$ kW, which requires a battery mass of $m_b = 4.3$ kg and motor mass of $m_p \approx 2.2$ kg using the assumed power-to-weight ratio λ_m. All together, this leads to a multicopter weight of $m_m = m_0 + m_b + m_p \approx 7$ kg.

III. Simulation Models

A. Multicopter

The multicopter is modeled as a point mass with three translational degrees of freedom. The rotational dynamics have been neglected because they do not have a major influence on the presented results in this paper. This is especially due to the fact that, in this application, no high dynamic maneuvers are flown, and the multicopter remains most of the time in a quasi-hover state. A full six-degree-of-freedom model can be included in the future, as soon as relevant geometric, aerodynamic, and motor characteristics are derived from a real prototype. Note that the size estimation of the multicopter in the previous section is conservative enough, such that stabilizing the attitude dynamics of the multicopter is possible with the allocated thrust reserves. The governing equations of motion can be derived by Newton's second law of motion [8] and are given by

$$\begin{aligned}(\dot{\boldsymbol{p}}_m)_W &= (\boldsymbol{v}_{m,k})_W,\\ (\dot{\boldsymbol{v}}_{m,k})_W &= \frac{1}{m_m}(\boldsymbol{F}_{m,\text{tot}})_W\end{aligned} \tag{9}$$

where $(\boldsymbol{p}_m)_W \in \mathbb{R}^{3\times1}$ and $(\boldsymbol{v}_{m,k})_W \in \mathbb{R}^{3\times1}$ represent the position and kinematic velocity of the center of gravity in the fixed reference frame W, respectively. The total force vector $(\boldsymbol{F}_{m,\text{tot}})_W \in \mathbb{R}^{3\times1}$ can be split into

$$(\boldsymbol{F}_{m,\text{tot}})_W = (\boldsymbol{F}_{m,a})_W + (\boldsymbol{F}_{m,g})_W + f(\boldsymbol{F}_{m,t})_W + (\boldsymbol{F}_{m,p})_W \tag{10}$$

where $(\boldsymbol{F}_{m,a})_W \in \mathbb{R}^{3\times1}$ represents the aerodynamic force; $(\boldsymbol{F}_{m,g})_W \in \mathbb{R}^{3\times1}$ represents the gravitational force; $(\boldsymbol{F}_{m,t})_W \in \mathbb{R}^{3\times1}$ represents

the force that is transmitted by the tether between kite and multicopter; and $(\boldsymbol{F}_{m,p})_W \in \mathbb{R}^{3\times 1}$ represents the propulsion force. Note that $f \in \{0, 1\}$ is set to zero if the kite and multicopter are detached and set to 1 otherwise. Because the multicopter is flying at low speeds, the drag and lift forces are negligibly small compared to the thrust and the disturbance induced by the kite; thus, a detailed aerodynamic model is omitted. The weight of the multicopter is defined by

$$(\boldsymbol{F}_{m,g})_W^T = (\,0 \quad 0 \quad -m_m g\,)_W \tag{11}$$

Because the rotational dynamics as well as the actuator dynamics are neglected, the orientation of the propulsion force vector is directly given by the desired flight direction calculated by the flight controller as described in Sec. IV, which is equivalent to the assumption of perfect and infinitely fast attitude and rate loops. If the attitude dynamics are included in the future, the orientation of the multicopter defines the orientation of the propulsion force vector, which is then given by

$$(\boldsymbol{F}_{m,p})_W = \boldsymbol{M}_{\mathrm{WB}} \begin{pmatrix} 0 \\ 0 \\ F_T \end{pmatrix}_B \tag{12}$$

where it is assumed that the resulting thrust force vector is perpendicular to the $x_B y_B$ plane of the multicopter body-fixed reference frame, and F_T represents the absolute value of the thrust force vector. The matrix $\boldsymbol{M}_{\mathrm{WB}} \in \mathbb{R}^{3\times 3}$ transforms a vector from the B frame into the W frame. It can be split into two transformation matrices $\boldsymbol{M}_{\mathrm{WO}}$ and $\boldsymbol{M}_{\mathrm{OB}}$, where the former is given by

$$\boldsymbol{M}_{\mathrm{WO}} = \begin{pmatrix} \cos\xi & \sin\xi & 0 \\ \sin\xi & -\cos\xi & 0 \\ 0 & 0 & -1 \end{pmatrix} \tag{13}$$

and hence depends on the wind direction ξ relative to the x axis of the north–east–down reference frame O. $\boldsymbol{M}_{\mathrm{OB}}$ represents the well-known transformation matrix between the B frame and the north–east–down reference frame O (see [9]).

The tether connection between the kite and the multicopter is modeled as a spring–damper element, where the force in the tether is given by

$$\begin{aligned}(\boldsymbol{F}_{m,t})_W = \mu(e)(k(e - l_s) \\ + d(\boldsymbol{t}^{\mathrm{km}})_W^T((\boldsymbol{v}_{m,k})_W - (\boldsymbol{v}_{k,k})_W))(\boldsymbol{t}^{\mathrm{km}})_W\end{aligned} \tag{14}$$

where the Euclidean distance e between the tether attachment point at the kite $(\boldsymbol{p}_k^B)_W$ and the attachment point at the multicopter $(\boldsymbol{p}_m)_W$ is given by

$$e = \|(\boldsymbol{p}_m)_W - (\boldsymbol{p}_k^B)_W\|_2 \tag{15}$$

The direction of the tether force is defined by

$$(\boldsymbol{t}^{\mathrm{km}})_W = -\frac{(\boldsymbol{p}_m)_W - (\boldsymbol{p}_k^B)_W}{\|(\boldsymbol{p}_m)_W - (\boldsymbol{p}_k^B)_W\|_2} \tag{16}$$

l_s is the length of the tether, k is the spring constant, d is the damping coefficient, $(\boldsymbol{v}_{k,k})_W$ is the kinematic kite velocity, $(\boldsymbol{v}_{m,k})_W$ is the multicopter speed, and $\mu(\epsilon)$ is a smoothed Heaviside function given by

$$\mu(e) = \min\left(\max\left(\frac{1}{\Delta_\epsilon} e + 1, 0\right), 1\right) \tag{17}$$

that drives the tether force to zero whenever the tether is not fully stretched. The function interpolates linearly between zero and 1, depending on the chosen slope $1/\Delta_\epsilon$. In this work, $\Delta_\epsilon = 0.001$ is chosen. The smoothing of the tether force turns out to be numerically more efficient because the tether force does not change infinitely fast between the taut and loose tether state. For the spring and damping constants, the same values as in [6] are used.

B. Kite

The dynamics of the kite are implemented in the simulation framework according to the model presented in [6]. A short overview of the model will be given in the following. For a detailed derivation of the equations of motion, please refer to [6]. The kite is modeled as a four-point particle system, where the individual particles are connected by spring–damper elements. The shape of the kite is approximated by two side surfaces and one top surface, where the center of each surface represents one particle point mass. Aerodynamic forces are calculated individually with respect to the local airflow at the locations of the two side particles and the top particle. The fourth particle is added to obtain a three-dimensional body with rotational inertia. The attachment of the tether that connects kite and multicopter coincides with the top surface particle. The steering behavior of the kite is modeled by changing the local angles of attack of the side surfaces differentially and proportional to the steering input [6]. This results in a differential change of the aerodynamic forces acting on the side particles, which induces a yaw moment that results in a turn rate. The steering behavior model is a great simplification compared to reality but is sufficient for the purpose in this paper. For a more realistic high-fidelity model, please refer to [10]. The coupled system of differential equations that describes the dynamics of the kite is obtained eventually by applying Newton's second law of motion for every particle point mass, which yields

$$\begin{aligned}(\dot{\boldsymbol{p}}_k^i)_W &= (\boldsymbol{v}_{k,k}^i)_W, \\ (\dot{\boldsymbol{v}}_{k,k}^i)_W &= \frac{1}{m_{k,i}} \cdot (\boldsymbol{F}_\Sigma^i)_W\end{aligned} \tag{18}$$

where i denotes the ith kite particle, and the resultant force is denoted by $(\boldsymbol{F}_\Sigma^i)_W$. The calculation of the specific forces that form the resultant force is discussed in detail in [6] and will not be repeated here. The only additional force that appears in the equations of motion in the present work is the tether force transmitted through the tether that connects the multicopter with the kite, as defined in Eq. (14). It is supposed that the attachment point coincides with point B as defined in [6].

C. Tether

The tether between ground station and kite is modeled as a n-particle system and is also adapted from [6]. The individual segments are modeled as spring–damper elements according to Eq. (14). In contrast to the connection between the multicopter and the kite, the tether between kite and ground station has a variable length. This will be modeled by simultaneously changing the lengths of the segments during the reel-out phase. Analogous to the kite particles, for every tether particle, Newton's second law will be applied. For particles 2 to $n_p - 1$, where n_p is the number of particles, this yields

$$\begin{aligned}(\dot{\boldsymbol{p}}_t^i)_W &= (\boldsymbol{v}_{t,k}^i)_W, \\ (\dot{\boldsymbol{v}}_{t,k}^i)_W &= \frac{1}{m_{t,i}}((\boldsymbol{F}_g^i)_W + (\boldsymbol{F}_a^i)_W + (\boldsymbol{F}_{t,i-1}^i)_W + (\boldsymbol{F}_{t,i+1}^i)_W)\end{aligned} \tag{19}$$

$(\boldsymbol{F}_{\mathrm{g}}^i)_W$ and $(\boldsymbol{F}_a^i)_W$ denote the gravitational and the aerodynamic force for particle i, respectively. A detailed derivation of these forces can again be found in [6]. $(\boldsymbol{F}_{t,i-1}^i)_W$ and $(\boldsymbol{F}_{t,i+1}^i)_W$ represent the spring–damper forces of the connecting tether segments. For the first particle $i = 1$, the lower spring–damper force is replaced by the force as experienced by the winch, and for the last particle $i = n$, the upper

spring–damper force is replaced by the three spring–damper forces that model the bridle system.

D. Ground Station

In this work, only the mechanical part of the ground station (i.e., the winch) is modeled as a simple scalar second-order system given by

$$\dot{\theta}_w = \omega,$$
$$\dot{\omega}_w = \frac{1}{J_w}(r_w \|(\boldsymbol{F}^1_{t,1})_W\|_2 - \nu_w \dot{\theta}_w + M_c) \tag{20}$$

where r_w is the drum radius, ν_w is the friction coefficient, $\|(\boldsymbol{F}^1_{t,1})_W\|_2$ is the absolute tether force of the first tether segment, and M_c is the control moment. System-specific parameters are listed in [6]. The overall tether length is given by

$$l_t = r_w \theta_w \tag{21}$$

E. Wind Shear and Turbulence Models

To simulate the launching and landing maneuvers in a realistic wind environment, a Dryden turbulence model has been superimposed to a shear wind field model. Both models are implemented according to MIL-F-8785C for category C flight phases, which incorporate takeoff and landing maneuvers of aircraft. Therefore, the model seems to be adequate in the analyzed launching and landing context of this work. According to the specification the shear model is given by

$$v_w = W_{20} \frac{\ell_n(h/z_0)}{\ell_n(20/z_0)} \tag{22}$$

where W_{20} is the wind speed at 6 m, h is the current altitude in feet, and $z_0 = 0.15$ is a parameter chosen according to the specification. If it is assumed that Eq. (22) reflects the local wind profile accurately, then it can also used to estimate the altitude at which a certain wind speed is expected if no other information about the wind profile is available. In this case, it is assumed that W_{20} is measurable. The wind shear field for different reference wind speeds is depicted in Fig. 8.

IV. Controller Design

A. Multicopter Flight-Path Controller

In this section, the control strategy will be presented, and the control laws will be derived. Overall, the launching procedure can be divided into three phases. In the first phase, the multicopter takes off while the kite remains in the initial state until the tether between multicopter and kite is taut. In the second phase, the multicopter drags the kite along the launching path until the specified operational altitude is reached. At the same time, the winch reels out the tether using the control approach presented in Sec. IV. As soon as the multicopter reaches the operational altitude, the kite will be released and the tether length set point will be set to the previous value, which sets the reeling-out speed to zero. The multicopter continues following the landing path and the kite is steered toward its parking position according to Eq. (1). As soon as the multicopter has landed, the launching phase is terminated, and the kite goes into power-production mode.

The landing maneuver will be carried out inversely. As soon as the landing mode is triggered, the kite will be steered to the parking position. From there, it will be pulled toward the ground station using a force-feedback control approach. The force-feedback control allows to adapt the reeling-out speed to the wind speed as experienced by the kite. For low wind speeds, the kite will be pulled faster to the ground station; for high wind speeds, the reeling-in speed will be decreased. Note that the same control strategy is used if the kite is launched without multicopter assistance.

For the multicopter flight control architecture, a cascaded structure is chosen. Because highly curved flight paths are not required during the launching and the landing procedure, a path-following controller that enables the multicopter to follow straight line segments connected with circular orbits with a defined velocity profile is sufficient. Because the rotational dynamics of the multicopter are neglected in this work, no inner-loop controller will be derived. However, because of the modularity of the cascade structure, an attitude and rate loop can be added effortlessly in the future as soon as more model data become available. The output of the path-following control module will be the required attitude that the inner loop has then to track.

1. Path Planner

In this section, the launching path will be defined, consisting of straight line segments connected with circle segments to achieve smooth transitions from one line segment to another. The general appearance of the reference flight path with a path angle of $\gamma = 60$ deg is depicted in Fig. 9. The solid lines represent the flight-path segments connected by the waypoints indicated with the circular markers. During the first part of the launching phase, the multicopter follows a vertical path segment before transitioning into the inclined path segment via two circle segments that start and end tangentially to the two adjacent straight line segments. As soon as the multicopter reaches the release altitude, which is indicated by the cross, the kite is released, and the multicopter follows another circular orbit and a final straight line descend path segment. Note that the tangential transitioning into the circular orbit after the kite release helps to control the sudden acceleration that the multicopter experiences after the detachment. To keep the path planning as simple as possible,

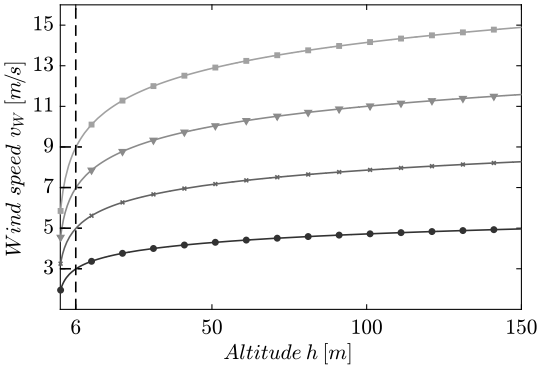

Fig. 8 Wind shear with $W_{20} = 3$ m/s (circles), 5 m/s (crosses), 7 m/s (triangles), and 9 m/s (squares).

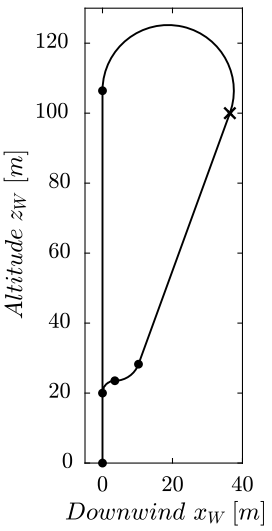

Fig. 9 Visualization of an example reference launching path in the $x_W z_W$ plane.

a minimal representation of the reference flight path is developed. More specifically, the path is fully defined by the release altitude h_r, the path angle of the straight line segment until the release altitude (γ_l), and the altitude of the initial vertical segment h_i. The former two values are chosen based on the results in Sec. II; the latter is chosen according to spatial constraints at the launching side. The radii $r_j, j \in \{1, 2, 3\}$ as well as the centers of the circular segments $(\boldsymbol{p}_{c,j})_W$ can be calculated based on the geometry of the path. The first circular segment is defined by

$$\begin{aligned} r_1 &= h_i \tan\left(\frac{\pi}{4} - \frac{\gamma_l}{2}\right), \\ (\boldsymbol{p}_{c,1})_W^T &= \begin{pmatrix} r_1 & 0 & h_i \end{pmatrix} \end{aligned} \tag{23}$$

The derivation of r_2 and $(\boldsymbol{p}_{c,2})_W$ requires intermediate steps. First, the waypoint between the first and second circular segment is calculated according to

$$(\boldsymbol{w}_3)_W^T = (\boldsymbol{p}_{c,1})_W^T + \begin{pmatrix} 0 & 0 & r_1 \end{pmatrix}_W \tag{24}$$

The subsequent waypoint can be calculated with

$$(\boldsymbol{w}_4)_W = (\boldsymbol{w}_3)_W + \begin{pmatrix} 1 + \cos\gamma_l \\ 0 \\ \sin\gamma_l \end{pmatrix}_W \left(\frac{w_{3,z}}{\tan\gamma_l} - w_{3,x}\right) \tag{25}$$

where $w_{3,x}$, $w_{3,z}$ represent the x_W and y_W components of $(\boldsymbol{w}_3)_W$, respectively. The radius and origin of the second orbit are then given by

$$\begin{aligned} r_2 &= \frac{w_{4,x} - w_{3,x}}{\sin\gamma_l}, \\ (\boldsymbol{p}_{c,2})_W^T &= (\boldsymbol{p}_{c,1})_W^T + \begin{pmatrix} 0 & 0 & r_1 + r_2 \end{pmatrix}_W \end{aligned} \tag{26}$$

where $w_{4,x}$ is the x_W component of $(\boldsymbol{w}_4)_W$. The radius and origin of the third orbit can be calculated according to

$$\begin{aligned} r_3 &= \frac{h_r}{\sin\gamma_l} \tan\left(\frac{\pi}{4} - \frac{\gamma_l}{2}\right), \\ (\boldsymbol{p}_{c,3})_W^T &= \begin{pmatrix} r_3 & 0 & \frac{h_r}{\sin\gamma_l} \end{pmatrix} \end{aligned} \tag{27}$$

The remaining waypoints are given by

$$\begin{aligned} (\boldsymbol{w}_1)_W^T &= \begin{pmatrix} 0 & 0 & 0 \end{pmatrix}_W, \\ (\boldsymbol{w}_2)_W^T &= \begin{pmatrix} 0 & 0 & h_i \end{pmatrix}_W, \\ (\boldsymbol{w}_5)_W^T &= \begin{pmatrix} \frac{h_r}{\tan\gamma_l} & 0 & h_r \end{pmatrix}_W, \\ (\boldsymbol{w}_6)_W^T &= \begin{pmatrix} 0 & 0 & \frac{h_r}{\sin\gamma_l} \end{pmatrix}_W \end{aligned} \tag{28}$$

The path parameters h_r and γ_l are determined according to the results in Sec. II. The path inclination is chosen such that the kite will be launched below the parking equilibrium elevation angle because this will result in a tangential motion toward the equilibrium position as soon as the kite is detached from the multicopter. The expected parking equilibrium angle can be determined based on the results in Sec. II. Because the wind field is, in the general case, not known at all altitudes, only bounds on the launching elevation can be given. Because the multicopter is designed such that it can lift the kite without relying on a minimum wind speed, the operational envelope can be enlarged such that the kite system can also be launched in low-wind conditions in ground proximity. The condition that, at release altitude, the wind speed must be higher or equal 8 m/s will be used to determine the release altitude. Note that this yields a conservative boundary condition according to the discussion in Sec. II. The release altitude can be determined based on either a wind model or an online estimation of the wind speed at the kite. The latter one would additionally require that the reference path is adapted online as a function of the estimated wind field. The online estimation of the wind field is not part of this work; hence, it is assumed that a model for the wind field is available (e.g., from previous wind field measurements or estimations and used to predict the release altitude at which $v_w \geq 8$ m/s is to be expected). The proposed methodology will be carried out using the example wind shear model depicted in Fig. 8. Using this model, it can be observed that, for low wind speeds (e.g., $W_{20} = 3$ m/s), the required release altitude might become unfeasible due to onboard power constraints defined by the design choices presented in Sec. II.B. Therefore, it is necessary to also constrain the maximum release altitude in order not to violate the maximum available flight time given a specific velocity trajectory. In this work, the launching phase of the kite is estimated to take at most 180 s, which represents a time constraint for the launching phase that can be transformed into a maximum path length requirement. With a launching velocity of 1 m/s, the maximum launching distance can be calculated to be 180 m. Note that this is a conservative bound because it assumes that the multicopter is flying with full throttle during the entire launching phase. The constraint for the maximum release altitude depends then only on the path angle, which is conservatively chosen based on the measured ground wind speed. Assuming conservatively that $\Theta_\tau = 0$ deg, the minimum path angle is approximately $\gamma_l = 72$ deg, which corresponds to a wind speed of $v_{w,\min} \approx 8$ m/s. The maximum release altitude is then given by $h_{r,\max} = 180 \sin(\gamma_l) \approx 170$ m.

With the example shear wind model as described by Eq. (22), the minimum reference wind velocity at 6 m altitude can be calculated by solving the wind model for W_{20} with $v_w = 8$ m/s and $h_r = 170$ m, which yields $W_{20,\min} = 4.76$ m/s. If this is done for different release altitudes, the results in Fig. 10 are obtained. Note that the hatched rectangular areas represent unfeasible solutions because they violate the maximum altitude constraint. For the subsequent simulations, a theoretical boundary of 5 m/s is chosen because it leads to a much lower release altitude of 126 m instead of 176 m, where it would be required that the multicopter tracks the velocity command of 1 m/s perfectly in order not to violate the launching time constraint of 180 s. Note that, with the given wind profile, this would enlarge the operational launching envelope from 8 to 5 m/s, conservatively.

For the landing, no prescribed landing path is defined. The reason is that only the radial motion of the kite can be controlled actively by the winch. However, from the equilibrium analysis in Sec. II, it can be deduced that, for $v_r < 0$, the kite has the tendency to reach an equilibrium elevation angle if the reeling-in speed and the wind speed form a feasible solution. Because the kite starts from an equilibrium, deviations from this equilibrium due to external disturbances will always induce a motion in the x_τ direction toward an equilibrium point. Connecting all the equilibrium points along the wind shear profile from the parking altitude to the ground, given a certain reeling-in speed, results in a virtual landing flight path that will be followed automatically due to the inherent flight physics of the kite. Theoretically, this makes the landing of the kite rather simple if the

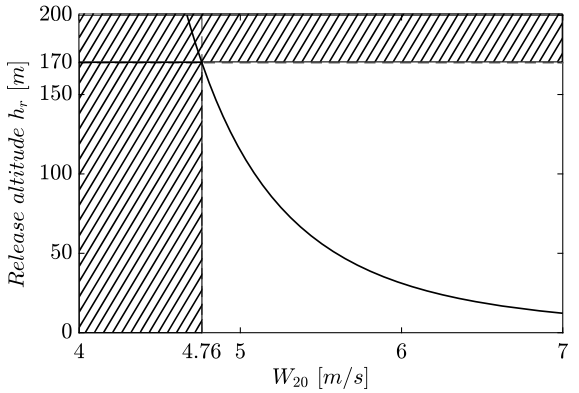

Fig. 10 Required launching altitude h_r with $v_w = 8$ m/s as a function of W_{20}.

wind speed is sufficiently high. To further improve the robustness, the reeling-in speed is adjusted according to the measured tether force on the ground. The landing performance will be assessed in Sec. V in a turbulent wind field.

2. Path-Following Controller

Because the path consists of several individual segments, a logic module is required that switches between the active path segments. The switching is triggered as soon as the multicopter reaches the current target waypoint. Smooth transitions onto the path are achieved by implementing a virtual target pursuit algorithm. In both cases, the current to-be-followed path segment is defined by the waypoint ahead $(\boldsymbol{w}_+)_W$ and the previous waypoint $(\boldsymbol{w}_-)_W$. In the case that $(\boldsymbol{w}_+)_W$ and $(\boldsymbol{w}_-)_W$ are connected with a straight line, the path segment vector is given by

$$(\boldsymbol{s}_*)_W = (\boldsymbol{w}_+)_W - (\boldsymbol{w}_-)_W \tag{29}$$

and the relative position between the multicopter and the previous waypoint $(\boldsymbol{w}_-)_W$ is given by

$$(\boldsymbol{p}_{\mathrm{wm}})_W = (\boldsymbol{p}_m)_W - (\boldsymbol{w}_-)_W \tag{30}$$

To calculate the virtual target on the path, the current multicopter position needs to be projected onto the path. In case a straight line has to be followed, the closest point is simply given by the normal projection according to

$$(\boldsymbol{p}_{m,\perp})_W = \frac{(\boldsymbol{p}_{\mathrm{wm}})_W^T (\boldsymbol{s}_*)_W}{(\boldsymbol{s}_*)_W^T (\boldsymbol{s}_*)_W} (\boldsymbol{s}_*)_W \tag{31}$$

The virtual target that the multicopter has to follow is then obtained by moving the normal projection forward in the positive segment direction according to

$$(\boldsymbol{p}_{\mathrm{vt}})_W = (\boldsymbol{w}_-)_W + (\|(\boldsymbol{p}_{\mathrm{m},\perp})_W\|_2 + \Delta_{\mathrm{VT}}) \frac{(\boldsymbol{s}_*)_W}{\|(\boldsymbol{s}_*)_W\|} \tag{32}$$

where Δ_{VT} is a tuning parameter that defines how aggressive the path-following controller will guide the multicopter onto the path. If $\Delta_{\mathrm{VT}} \to 0$, the multicopter will be guided perpendicular onto the path, which results eventually in oscillations around the path due to the inertia of the system. If Δ_{VT} is too large, the perpendicular distance error component will only be reduced slowly. Hence, a tradeoff between the two scenarios has to be made; for the results in this work, $\Delta_{\mathrm{VT}} = 0.5$ resulted in a reasonable path-following performance.

To determine the position of the virtual target on a circular orbit, the orthogonal projection $(\boldsymbol{p}_{m,p})_{C,j}$ in the circle frame C, j is calculated according to

$$\begin{aligned}
(\boldsymbol{p}_m)_{C,j} &= (\boldsymbol{p}_m)_W - (\boldsymbol{p}_{c,j})_W, \\
(\boldsymbol{p}_{m,2})_{C,j} &= 0, \\
(\boldsymbol{p}_{m,p})_{C,j} &= (\boldsymbol{p}_m)_{C,j}, \\
(\boldsymbol{p}_{m,p})_{C,j} &= \frac{(\boldsymbol{p}_{m,p})_{C,j}}{\|(\boldsymbol{p}_{m,p}), C, j\|_2} r_j
\end{aligned} \tag{33}$$

which represents the closest point on the circle relative to the current position. To obtain the virtual target, the projected position has to be rotated by a user-specified angle Δ_c. Depending on the circle segment, Δ_c has to be chosen positive or negative such that the multicopter follows the orbit in clockwise or counterclockwise direction. For the reference path depicted in Fig. 9, $|\Delta_c| = 6$ deg is chosen where the first circular segment is followed in the clockwise direction, and the remaining two segments are followed in the counterclockwise direction. The virtual target to be followed is eventually transformed back into the W reference frame according to

$$(\boldsymbol{p}_V)_W = \begin{pmatrix} \cos\Delta & 0 & \sin\Delta \\ 0 & 1 & 0 \\ -\sin\Delta & 0 & \cos\Delta \end{pmatrix} (\boldsymbol{p}_{m,p})_{C,j} + (\boldsymbol{p}_{c,j})_W \tag{34}$$

Note that, in both cases (straight line and circular orbit following), additional constraint are implemented that ensure that the virtual target is not placed farther than the waypoint ahead.

The desired velocity vector that the controller has to track is finally given by

$$(\boldsymbol{v}_{\mathrm{cmd},k})_W = v_{\mathrm{cmd},k} \frac{(\boldsymbol{p}_V)_W - (\boldsymbol{p}_m)_W}{\|(\boldsymbol{p}_V)_W - (\boldsymbol{p}_m)_W\|_2} \tag{35}$$

where $v_{\mathrm{cmd},k}$ is the desired absolute kinematic velocity. Based on the error between the real and the desired velocity vector, the required acceleration that guides the multicopter onto the path can be calculated. The current velocity tracking error and its time derivative are defined as

$$\begin{aligned}
(\boldsymbol{e}_v)_W &= (\boldsymbol{v}_{r,k})_W - (\boldsymbol{v}_{m,k})_W, \\
(\dot{\boldsymbol{e}}_v)_W &= (\boldsymbol{a}_{r,k})_W - (\dot{\boldsymbol{v}}_{m,k})_W
\end{aligned} \tag{36}$$

$(\dot{\boldsymbol{v}}_{m,k})_W$ can be substituted by Eq. (9), where only the known forces will be considered for the derivation of the control law. All the remaining uncertainties are summarized in Δ_e according to

$$\Delta_e = (\boldsymbol{F}_{m,a})_W + f(\boldsymbol{F}_{m,t})_W \tag{37}$$

including the induced disturbance by the kite as well as the aerodynamic force. The resulting path-following error dynamics are then given by

$$(\dot{\boldsymbol{e}}_v)_W = (\boldsymbol{a}_{r,k})_W - \frac{1}{m_m}((\boldsymbol{F}_{m,g})_W + (\boldsymbol{F}_{m,p})_W + \Delta_e) \tag{38}$$

This yields the required thrust vector $(\boldsymbol{F}_{\mathrm{cmd},p})_W$:

$$(\boldsymbol{F}_{\mathrm{cmd},p})_W = m_m(\boldsymbol{\nu}_r)_W - (\boldsymbol{F}_{m,g})_W \tag{39}$$

where $(\boldsymbol{\nu}_r)_W$ represents the desired acceleration given by

$$(\boldsymbol{\nu}_r)_W = (\boldsymbol{a}_{r,k})_W + \boldsymbol{K}_v(\boldsymbol{e}_v)_W \tag{40}$$

with a diagonal positive feedback gain $\boldsymbol{K}_v \in \mathbb{R}^{3\times3}$, and $(\boldsymbol{a}_{r,k})_W$ represents the desired acceleration that can be calculated with a first-order reference filter defined by

$$(\boldsymbol{a}_{r,k})_W = -\frac{1}{\tau_r}(\boldsymbol{v}_{r,k})_W + \frac{1}{\tau_r}(\boldsymbol{v}_{\mathrm{cmd},k})_W \tag{41}$$

where τ_r represents the time constant of the filter. The choice of the time constant is usually constrained by the time constants of the inner-loop dynamics and the bandwidth of the actuator dynamics. Because both inner-loop and actuator dynamics are neglected, no further constraints on τ_r are imposed. The pseudocontrol law in Eq. (39) ensures stable error dynamics, assuming that Δ_e is bounded, which is trivial to see from Eq. (42):

$$(\dot{\boldsymbol{e}}_v)_W + \boldsymbol{K}_v(\boldsymbol{e}_v)_W = -\Delta_e/m_m \tag{42}$$

Based on $(\boldsymbol{F}_{\mathrm{cmd},p})_W$, the desired attitude set points for the inner-loop controller can be calculated similar to the approach presented for instance in [11] using the relation

$$\boldsymbol{M}_{\mathrm{OW}}(\boldsymbol{F}_{\mathrm{cmd},p})_W = \begin{pmatrix} f_x \\ -f_y \\ -f_z \end{pmatrix}_O = \boldsymbol{M}_{\mathrm{OB}} \begin{pmatrix} 0 \\ 0 \\ -\|(\boldsymbol{F}_{\mathrm{cmd},p})_W\|_2 \end{pmatrix}_B \tag{43}$$

It is again assumed without restriction to generality that the wind direction coincides with the north direction. The desired roll and pitch angles can then be calculated by solving Eq. (43) for Φ_{cmd} and Θ_{cmd}, which yields

$$\Phi_{\text{cmd}} = -\arcsin\left(\frac{1}{\|(\boldsymbol{F}_{D,p})_W\|_2}\left(f_x \sin\Psi_{\text{cmd}} + f_y \cos\Psi_{\text{cmd}}\right)\right),$$
$$\Theta_{\text{cmd}} = \arctan\left(-\frac{1}{f_z}\left(f_x \cos\Psi_{\text{cmd}} - f_y \sin\Psi_{\text{cmd}}\right)\right) \tag{44}$$

The heading angle Ψ_{cmd} can be chosen arbitrarily. The tuple $(\Phi_{\text{cmd}}, \Theta_{\text{cmd}}, \Psi_{\text{cmd}})$ will be the input to the attitude control loop. Because the attitude and rate dynamics are neglected thus far, Eq. (44) serves as an interface that can conveniently be connected to a future attitude control loop. Because of the high forces that the kite can generate, it is likely that the multicopter actuators saturate during the launching and landing phase. Although actuator dynamics are not yet implemented in the simulation framework, the available thrust is still limited based on the multicopter design decisions in Sec. II.B. To generate feasible reference trajectories and to prevent integrator windup in case of saturation, pseudocontrol hedging [9] is implemented.

B. Kite Attitude Controller

Kite power systems are usually controlled on the unit sphere, where the radial and tangential motions are assumed to be decoupled. In this case, the course controller tracks a reference course χ_τ on the moving tangential plane τ while the winch controller controls the movement in radial direction z_τ (cf. Fig. 3). During the launching, the kite has ideally no tangential movement, which means that the course in the tangential plane is not defined. In fact, the translational movement of the kite is entirely controlled by the winch and the multicopter. The control objective for the kite attitude controller will be to keep the kite oriented into the wind by controlling the tangential plane heading angle $\Psi_{\tau,c}$ to 0 deg.

Based on experimental data and kinematics, a correlation between the steering input and the course rate can be derived [7]. Because the sideslip angle is negligible due to the weathercock stability of the kite, the heading rate is equal to the course rate, which allows a straightforward adoption of the course rate law to derive the kite attitude controller for the launching and landing phase. The tangential plane heading angle that will be tracked during launching and landing can be calculated from the measured Euler angles using the relationship

$$\boldsymbol{M}_{\tau B}(\Psi_\tau, \Theta_\tau, \Phi_\tau) = \boldsymbol{M}_{\tau W}(\lambda, \phi)\boldsymbol{M}_{\text{WO}}(\xi)\boldsymbol{M}_{\text{OB}}(\Psi, \Theta, \Phi) \tag{45}$$

Comparing the general structure of $\boldsymbol{M}_{\tau B}$, which is equal to the structure of $\boldsymbol{M}_{\text{OB}}$, with the right-hand side allows to determine the attitude of the kite with respect to the tangential frame as follows:

$$\Phi_\tau = \arctan 2(\boldsymbol{M}_{B\tau,23}, \boldsymbol{M}_{B\tau,33}),$$
$$\Theta_\tau = \text{asin}(-\boldsymbol{M}_{B\tau,13}),$$
$$\Psi_\tau = \arctan 2(\boldsymbol{M}_{B\tau,12}, \boldsymbol{M}_{B\tau,11}) \tag{46}$$

where $\boldsymbol{M}_{B\tau,ij}$ denotes the component of $\boldsymbol{M}_{B\tau}$ in the ith row and jth column. In the simulation, the orientation of the kite in terms of Euler angles Ψ, Θ, and Φ is given by the relative position of the four particles as defined in [6]. An orthonormal basis representing the kite body-fixed frame B is then given by

$$(\boldsymbol{z}_B)_W = \frac{(\boldsymbol{p}_k^0)_W - (\boldsymbol{p}_k^B)_W}{\|(\boldsymbol{p}_k^0)_W - (\boldsymbol{p}_k^B)_W\|},$$
$$(\boldsymbol{y}_B)_W = \frac{(\boldsymbol{p}_k^C)_W - (\boldsymbol{p}_k^D)_W}{\|(\boldsymbol{p}_k^C)_W - (\boldsymbol{p}_k^D)_W\|},$$
$$(\boldsymbol{x}_B)_W = (\boldsymbol{y}_B)_W \times (\boldsymbol{z}_B)_W \tag{47}$$

with

$$(\boldsymbol{p}_0)_W = 0.5((\boldsymbol{p}_C)_W + (\boldsymbol{p}_D)_W) \tag{48}$$

The transformation matrices in Eq. (45) can then be calculated according to

$$\boldsymbol{M}_{\text{BO}} = \boldsymbol{M}_{\text{BW}}\boldsymbol{M}_{\text{WO}} = \begin{pmatrix} (\boldsymbol{x}_B)_W^T \\ (\boldsymbol{y}_B)_W^T \\ (\boldsymbol{z}_B)_W^T \end{pmatrix}\begin{pmatrix} \cos\xi & \sin\xi & 0 \\ \sin\xi & -\cos\xi & 0 \\ 0 & 0 & -1 \end{pmatrix} \tag{49}$$

with $\boldsymbol{M}_{\text{OB}} = \boldsymbol{M}_{\text{BO}}^T$ and

$$\boldsymbol{M}_{W\tau} = \begin{pmatrix} -\sin\phi\cos\lambda & -\sin\lambda & -\cos\phi\cos\lambda \\ -\sin\phi\sin\lambda & \cos\lambda & -\cos\phi\sin\lambda \\ \cos\phi & 0 & -\sin\phi \end{pmatrix} \tag{50}$$

The steering correlation will be based on the relationship between the rotational rate of the body-fixed frame relative to the tangential plane frame τ, which is given by

$$(\boldsymbol{\omega}^{\text{OB}})_B = (\boldsymbol{\omega}^{W\tau})_B + (\boldsymbol{\omega}^{\text{WO}})_B + (\boldsymbol{\omega}^{\tau B})_B \tag{51}$$

where $(\boldsymbol{\omega}^{\text{OB}})_B$ is measured by the onboard inertial measurement unit (IMU). The transport rate $(\boldsymbol{\omega}^{\text{WO}})_B$ can be neglected in this application; hence, the remaining rates can be written as

$$\begin{pmatrix} p \\ q \\ r \end{pmatrix}_B = \boldsymbol{M}_{\text{BW}}\begin{pmatrix} \dot\lambda\sin\phi \\ -\dot\phi\cos\lambda \\ \dot\phi \end{pmatrix}_W + \begin{pmatrix} \dot\Phi_\tau - \dot\Psi_\tau\sin\Theta_\tau \\ \dot\Theta_\tau\cos\Phi_\tau + \dot\Psi_\tau\sin\Phi_\tau\cos\Theta_\tau \\ -\dot\Theta_\tau\sin\Phi_\tau + \dot\Psi_\tau\cos\Phi_\tau\cos\Theta_\tau \end{pmatrix}_B \tag{52}$$

with

$$\dot\lambda = \frac{v_k}{\|(\boldsymbol{p}_k^G)_W\|_2\cos\phi},$$
$$\dot\phi = \frac{u_k}{\|(\boldsymbol{p}_k^G)_W\|_2} \tag{53}$$

where u_k and v_k are the x_τ and y_τ components of the kinematic velocity vector of the kite in the tangential plane frame denoted with $\boldsymbol{v}_{k,\tau}$ in Fig. 11, and $(\boldsymbol{p}_k^G)_W$ denotes the position of the kite's center of gravity. Because during the launching and the landing phase the movement of the kite in the tangential plane is negligible, it can be assumed that $\dot\lambda \approx \dot\phi \approx 0$. The third row of Eq. (52) can then be simplified to

$$r = -\dot\Theta_\tau\sin\Phi_\tau + \dot\Psi_\tau\cos\Phi_\tau\cos\Theta_\tau \tag{54}$$

The angle Φ_τ is usually negligibly small, hence

$$r = \dot\Psi_\tau\cos\Theta_\tau \tag{55}$$

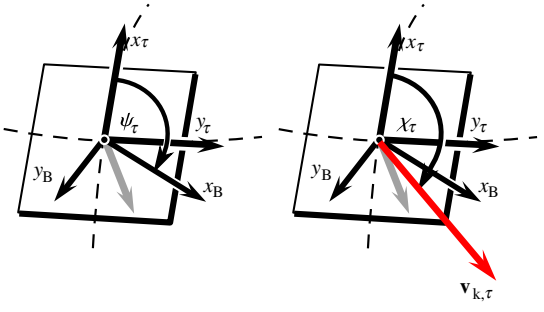

Fig. 11 Definition of tangential plane heading Ψ_τ and course χ_τ.

Using the steering correlation as presented in [7], the model for the tangential plane heading rate is chosen to be

$$\dot{\Psi}_\tau = \frac{1}{\cos\Theta_\tau}\left(c_1 v_a u_s + c_2 \frac{(\boldsymbol{F}_{k,g})_W^T(\boldsymbol{y}_B)_W}{g}\right) \tag{56}$$

where u_s is the steering input, and $(\boldsymbol{F}_{k,g})_W^T(\boldsymbol{y}_B)_W$ can be calculated based on the attitude correlation of the kite according to Eq. (49) and is given by

$$(\boldsymbol{F}_{k,g})_W^T(\boldsymbol{y}_B)_W = \cos\Theta\sin\Phi m_k g \tag{57}$$

The coefficients c_1 and c_2 are calculated based on a linear regression as described in [7] and are kite-specific. During the launching and landing phase, the roll angle of the kite is close to zero (i.e., $\Phi \approx 0$), which further simplifies the steering-law model. Inverting the heading rate law and substituting the heading rate with a commanded heading rate as a pseudocontrol input yields

$$u_s = \frac{\cos\Theta_\tau \nu_{\Psi_\tau}}{c_1 v_a} \tag{58}$$

where ν_{Ψ_τ} is the pseudocontrol input defined by

$$\nu_{\Psi_\tau} = \dot{\Psi}_{\tau,r} + k_{p,\Psi_\tau} e_{\Psi_\tau} + k_{i,\Psi_\tau}\int_0^{t'} e_{\Psi_\tau}\,\mathrm{d}t \tag{59}$$

with the tracking error $e_{\Psi_\tau} = \Psi_{\tau,r} - \Psi_\tau$ and control gains $k_{p,\Psi_\tau}, k_{i,\Psi_\tau} > 0$. The reference heading rate is given by a scalar first-order reference filter:

$$\dot{\Psi}_{\tau,r} = -\frac{1}{\tau_\Psi}\Psi_{\tau,r} + \frac{1}{\tau_\Psi}\Psi_{\tau,c} \tag{60}$$

The parameter c_1 has to be determined based on experimental data and hence represents a multiplicative uncertainty that the feedback part in Eq. (59) has to account for.

C. Winch Controller

For the winch controller, two different modes are implemented. The first mode is used to control the winch during the multicopter-based launching, and the second mode is active for nonassisted launching as well as for landing. In the first mode, the winch controller is based on the model defined in Eq. (20). Within the scope of this paper, a simple linear quadratic regulator (LQR) with servomechanism is chosen [12]. The linear model for the controller synthesis is defined as

$$\begin{pmatrix}\dot{\theta}_w\\ \dot{\omega}_w\\ e_\theta\end{pmatrix} = \begin{pmatrix}0 & 1 & 0\\ 0 & -\nu_w/J_w & 0\\ -1 & 0 & 0\end{pmatrix}\begin{pmatrix}\theta_w\\ \omega_w\\ \int_0^t e_\theta\,\mathrm{d}\tau\end{pmatrix} + \begin{pmatrix}0\\ 1/J_w\\ 0\end{pmatrix} M_c \tag{61}$$

with $e_\theta = \theta_{w,\mathrm{cmd}} - \theta_w$. The feedback law is then given by

$$M_c = -\boldsymbol{K}_{\theta,p}\begin{pmatrix}\theta_w\\ \omega_w\end{pmatrix} + k_{\theta,i}\int_0^{t'} e_{\theta_w}\,\mathrm{d}t \tag{62}$$

with $\boldsymbol{K}_{\theta,p} \in \mathbb{R}^{1\times 2}$ and $k_{\theta,i} \in \mathbb{R}$ are the LQR gains. The feedback law allows to control the tether length according to Eq. (21). The set point $\theta_{w,c}$ is given by the current multicopter position and the dimensions of the kite and tether connection according to

$$\theta_{w,\mathrm{cmd}} = \frac{1}{r_w}(\|(\boldsymbol{p}_m)_W\|_2 - l_s - h_K - h_B) \tag{63}$$

where l_s is the constant length of the tether between multicopter and kite, $h_k = 2.23$ m is the height of the kite, and $h_b = 4.9$ m is the length of the bridle system. As a safety measure, the reeling-out speed will additionally be constrained by the launching velocity set point of the multicopter.

For the nonassisted launching and landing, the tether force is controlled. The set-point calculation for the reeling-out speed is based on a simple state machine with states $s = \{s_0, s_1, s_2\}$. If the measured tether force on the ground exceeds a threshold $T_{\mathrm{max},u}$, the state transition $s_0 \to s_1$ will be triggered, and the current reeling-out speed set point will be increased until the tether force drops below $T_{\mathrm{max},l}$ ($s_1 \to s_0$), where $T_{\mathrm{max},l} < T_{\mathrm{max},u}$ to avoid chattering. Similarly, if the tether force drops below a specified threshold $T_{\mathrm{min},l}$, the transition $s_0 \to s_2$ will be triggered, and a higher reeling-in speed will be commanded until the tether force exceeds $T_{\mathrm{min},u}$ ($s_2 \to s_0$), where $T_{\mathrm{min},u} > T_{\mathrm{min},l}$. The set points for $v_{r,\mathrm{cmd}}$ in each state are calculated according to

$$v_{r,\mathrm{cmd}} = \begin{cases} -K_p(|T - T_{\mathrm{max},l}|) & \text{if } T > T_{\mathrm{max},l} \wedge s = s_1\\ K_p(|T - T_{\mathrm{min},u}|) & \text{if } T < T_{\mathrm{min},u} \wedge s = s_2\\ \bar{v}_r & \text{if } T_{\mathrm{min},l} < T < T_{\mathrm{max},u} \wedge s = s_0\end{cases} \tag{64}$$

where $K_p = 0.01$, $T_{\mathrm{max},l} = 4$ kN, $T_{\mathrm{max},u} = 5$ kN, $T_{\mathrm{min},l} = 10$ N, and $T_{\mathrm{min},u} = 200$ N are chosen. As long as the tether force is between the maximum and minimum value ($s = s_0$), the winch will reel in or reel out with the nominal reeling-out speed $\bar{v}_r$ set by the operator, where $\bar{v}_r$ is either negative or positive during landing and launching, respectively. The speed controller is implemented analogously to the tether length controller. In this case, however, only the angular velocity commands from the state machine will be tracked by the proportional-integral (PI) controller.

V. Results

In this section, the feasibility of the proposed launching and landing methodology will be tested by means of numerical simulations employing the developed simulation models and controllers in Secs. III and IV. The section is subdivided into two parts, where, in the first part, results of launching simulations will be discussed, including VTOL with and without multicopter assistance. In the second part, results of landing simulations will be presented. The goal of both parts is to detect boundary conditions for automatic VTOL maneuvers for flexible wing kite power systems and to demonstrate the theoretical feasibility of the proposed methodology that can be used as a basis for the development and construction of an experimental setup.

A. Multicopter Launching

According to the measured wind speed at the reference altitude $h_r = 6$ m, the launching path angle and the release altitude will be determined based on the results in Sec. I. The feasibility of the multicopter-assisted launching will be verified at the boundaries using the following numerical simulation setup. For the simulation of the VTOL phases, a wind field as depicted in Fig. 12 with $W_{20} = 5$ m/s and an additional side wind component of $v_{y,w} = 2$ m/s is chosen. With a release altitude of $h_r = 130$ m, the results depicted in Fig. 13 are obtained, visualizing the altitude trajectory of the kite's center of gravity. It can be observed that, after the release, the kite stays airborne and converges to the parking elevation angle as expected. Also, the effect of a launching path inclination ϕ_{rel} that is slightly below the parking elevation angle ϕ_{eq} is visible, indicated in the slightly higher equilibrium altitude, corresponding to $\phi_{\mathrm{eq}} > \phi_{\mathrm{rel}}$, because the tether length is kept constant after the kite release. During the entire launching phase, the multicopter path-following controller is able to track the reference velocity accurately, despite the unknown induced disturbance of the kite, and hence guides the multicopter and kite along the predefined flight path robustly in the turbulent wind environment. After the kite is released at ≈143 s, the multicopter accelerates slightly, indicated by the peaks in Fig. 14, but recovers the tracking performance rapidly. Because of the lack of an aerodynamic

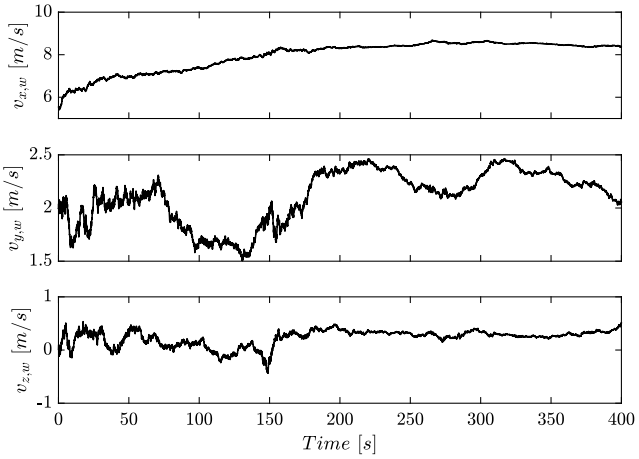

Fig. 12 Turbulent wind field selected for the multicopter launch.

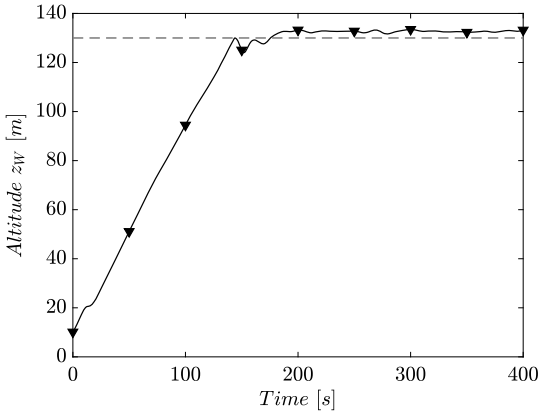

Fig. 13 Visualization of the kite's altitude trajectory in a turbulent wind field.

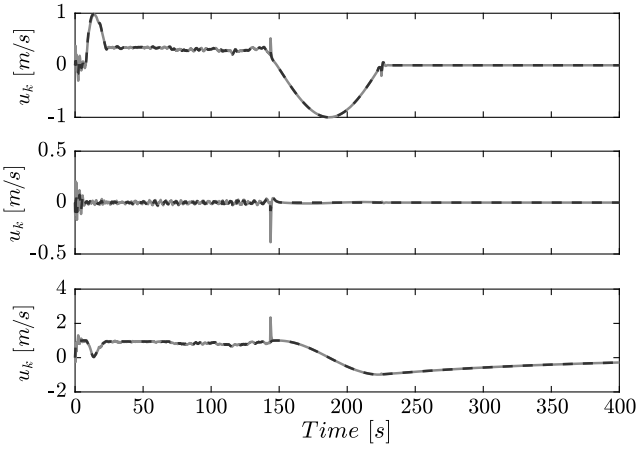

Fig. 14 Visualization of the velocity tracking performance.

model for the multicopter, the only disturbance the controller has to account for is represented by the kite. In the simulation, this leads only in the initial liftoff phase to deviations from the reference flight path. After the multicopter starts following the inclined flight-path segment defined by waypoints 4 and 5 (see Fig. 9), the deviations from the flight path are negligible. The initial and final segments of the multicopter flight path are depicted in Fig. 15. In Fig. 16, it can be observed that, as the wind speed increases with altitude, the induced disturbance of the kite acting on the multicopter raises, which has to

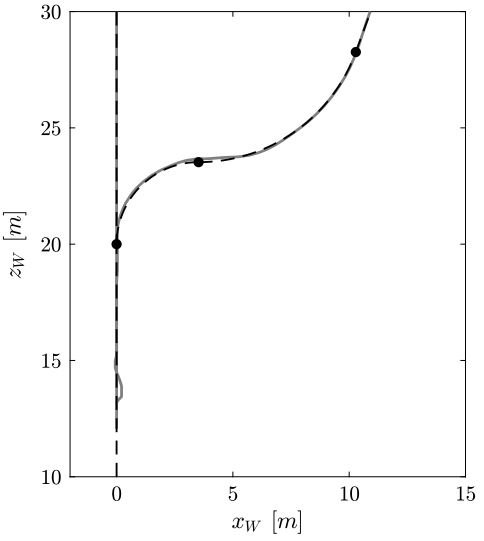

Fig. 15 Path-following performance of the multicopter during the initial and final approach phase.

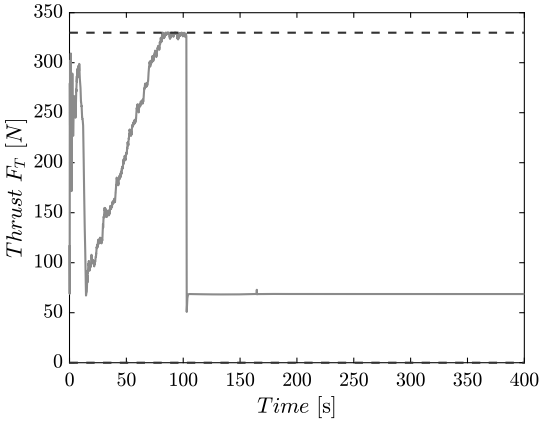

Fig. 16 Evolution of the total thrust of the multicopter.

be compensated with more thrust. Eventually, this leads to a saturation of the total thrust according to the design specifications in Sec. II.B. Saturation of the control input can usually cause integrator windup, which is prevented in this work using pseudocontrol hedging that essentially slows down the multicopter by adapting the generated reference velocity. Note that, in the future, the flight path could be further optimized such that the aerodynamic force of the kite would be exploited more beneficially to decrease the required thrust of the multicopter.

As can be observed in Fig. 17, the kite heading controller is able to keep the kite pointing toward the zenith position $\Psi_\tau = 0$, except the

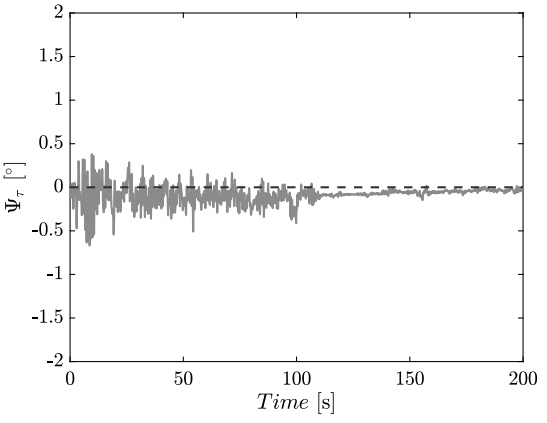

Fig. 17 Performance of the kite attitude controller.

small deviations due to the high-frequency disturbances induced by the wind turbulence especially in ground proximity (i.e., at the beginning of the launching phase, where the turbulence intensity is high).

Note that the flight path can also be chosen such that the kite will be guided along the equilibrium points given by the wind speed and the launching velocity profile according to Fig. 6. In this case, the tendency of the kite to leave the imposed launching path by the multicopter can be reduced, which reduces the disturbance induced by the kite aerodynamics on the multicopter. However, as has been discussed in Sec. II, higher radial velocities result in higher elevation angles. Hence, after the detachment of the kite, a tangential motion toward lower elevation angles will result. This can lead to high angles of attack that are not yet predictable by the model implemented in this work and are therefore not further investigated. Note that a forward acceleration instead of a backward acceleration after the release could be also beneficial for the transition into crosswind flight. In this case, the kite would not be parked after the release but directly steered into the traction phase figure.

B. Comparison of Assisted Versus Nonassisted Launching

In this section, the simple mast-based launching concept will be compared with the multicopter-based concept in a windfield with $W_{20} = 8$ m/s and $h_r = 100$ m. The mast-based concept relies simply on the lifting force of the kite that triggers the launching phase as soon as the lift force exceeds the weight of the kite. This approach obviously relies on sufficiently high wind speeds in ground proximity, in this case $v_w \geq 8$ m/s. For the wind field, $W_{20} = 8$ m/s and the same turbulence intensity as shown in Fig. 12 are chosen to produce the subsequent simulation results. The corresponding equilibrium elevation angle as a function of the reeling-out speed can be chosen according to Fig. 6. Furthermore, a nominal reeling-out speed equal to the commanded multicopter flight speed of 1 m/s is chosen to allow a proper comparison between the two approaches. Assuming that, in the initial kite position, $\Theta_\tau = 0$ deg, a mast inclination angle of $\approx$72 deg is chosen according to Fig. 6. The simulation results of the kite path in the $x_W z_W$ plane are shown in Fig. 18, where the trajectory indicated with the circles and crosses represent the multicopter-assisted and nonassisted case, respectively.

It can be observed that, apart from initial oscillations in the tangential direction, a launching performance similar to the case with multicopter assistance can be achieved. Small changes in the wind speed due to the turbulence lead to motions perpendicular to the virtual launching path. This is due to the fact that the kite is not forced to follow a path but instead tries to find a new equilibrium elevation angle depending on the current experienced apparent wind speed. This demonstrates the implicit control of the tangential motion of the kite, which makes the kite VTOL launch robust for sufficiently high wind speeds. Based on these observations, controlling only the radial motion of the nonassisted kite with the winch represents a feasible alternative to the multicopter-assisted launch, where the tangential movement can be controlled via the multicopter, hence making the launching performance less dependent on the wind speed.

To assess the conservatism of the minimum wind speed requirement for a nonassisted launch, simulations with $W_{20} < 8$ m/s and different nominal reeling-out speeds $\bar{v}_{\mathrm{ro}}$ have been conducted. Figure 19 shows the results of a nonassisted launching maneuver with $W_{20} = 7$ m/s. As expected, high nominal reeling-out speeds that do not comply with the suggested speeds in Fig. 6 deteriorate the launching performance due to the decreasing apparent wind speed and hence the decrease of the aerodynamic damping. As expected, the sensitivity toward the reeling-out speeds becomes less significant as the wind speeds increases. This can be observed in Fig. 20, which shows the resulting flight paths if the reference speed W_{20} is increased to 10 m/s. It can be concluded that the nonassisted kite launch should be carried out with small reeling-out speeds, which is essentially only limited by the accuracy of the winch speed controller, as discussed in Sec. II.

From a flight physical point of view, a lower nominal reeling-out speed leads to less oscillatory motions in the radial and tangential directions compared to a higher reeling-out speed in the same wind field, due to the increased aerodynamic damping, which is proportional to the square of the apparent wind speed. This limitation is not present in the case of the multicopter-assisted launch because the required aerodynamic damping necessary to control the kite's tangential movement is replaced by the control authority of the multicopter system, which in fact works best in lowwind conditions where the low aerodynamic damping of the kite results in smaller disturbances acting on the multicopter. Both concepts can thus be regarded as complementary where advantages and disadvantages are a function of the current wind speed.

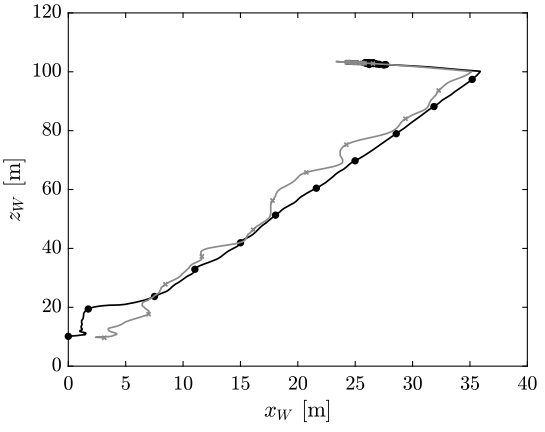

Fig. 18 Visualization of multicopter-assisted (circles) and nonassisted (crosses) flight path.

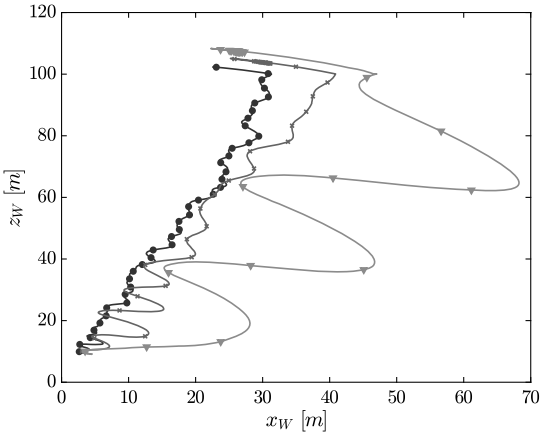

Fig. 19 Kite trajectories with $\bar{v}_r = 0.5$ m/s (circles), 1 m/s (crosses), and 2 m/s (triangles) and $W_{20} = 7$ m/s.

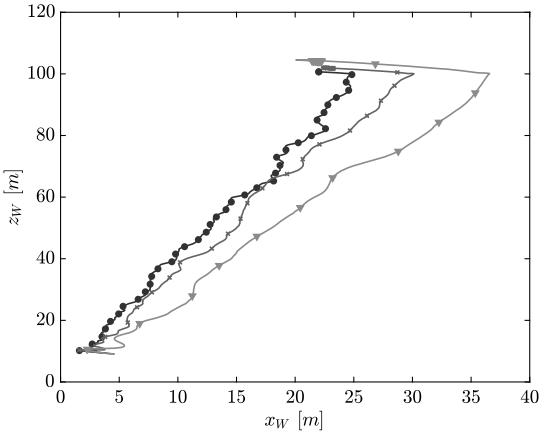

Fig. 20 Kite trajectories with $\bar{v}_r = 0.5$ m/s (circles), 1 m/s (crosses), and 2 m/s (triangles) and $W_{20} = 10$ m/s.

C. Landing

In this section, the controller performances during the landing will be analyzed. Supporting the kite landing with the multicopter is difficult to achieve because it would require that the multicopter catches the airborne kite autonomously, while the kite is in a parking equilibrium. Although this seems to be a major disadvantage of the present concept compared to the approach presented in [5], it will be shown that, with the presented winch controller, a predictable landing performance even without multicopter assistance can be achieved. The analysis of the landing phase is carried out similarly to the launching phase, and the controller performance will be tested in different wind conditions with turbulence and side wind components as well as with different nominal reeling-out speeds $\bar{v}_r$, which are chosen based on the presented boundary conditions in Sec. II. Note that, during the time that this research was conducted, no further design decisions regarding the mast or the reattachment process were available. Therefore, the landing phase will be defined as terminated as soon as a specific minimal tether length of 5 m is reached. The results of the first landing simulation study are depicted in Fig. 21, where three different wind fields have been simulated with a nominal reeling-in speed of $\bar{v}_r = -1$. In the case of $W_{20} = 7$ m/s and $W_{20} = 10$ m/s, the kite is pulled toward the ground with a constant speed after a short transition phase where the winch accelerates from $v_r = 0$ m/s to $v_r = -1$ m/s, as can be seen in Fig. 22. The pitch angle Θ_τ in both cases oscillates slightly around ≈ -5 deg and ≈ -3 deg, as can be observed in Fig. 23. The oscillations can be attributed to the turbulence contained in the wind field. In the low-wind-speed case (i.e., $W_{20} = 4$ m/s), the winch controller is actively adjusting the reeling speed to keep the measured tether force within the specified bounds. The continuous change in apparent wind speed leads eventually to significant oscillations in Θ_τ, which induce forward and backward motions of the kite, resulting in a strong coupling between the radial and the tangential dynamics. In fact, reeling in faster will first increase the apparent wind speed and hence the lift, which results in a higher tether tension. As a consequence, the tether will be reeled in again with a lower speed; hence, the apparent wind speed and consequently the tether tension drops, and the cycle starts all over again. Eventually, this leads to the observed oscillations in low-wind-speed conditions. It can be concluded that, although the force-feedback controller can adapt the reeling-in speed to sudden changes in the tether tension, it cannot overcome the fact that a certain wind speed in combination with a certain reeling-in speed is required to keep the kite airborne. A better landing performance can be obtained if, for low-wind conditions, a higher nominal reeling-in speed is selected based on Fig. 6 and the force-feedback controller is only used for disturbance compensation.

As has been discussed in the previous paragraph, in low-wind conditions (i.e., $v_w < 8$ m/s), the winch has to actively adapt the reeling-in speed to keep the tether taut. However, if too-high reeling-in speeds are selected, this can lead to overshoots with respect to the ground station that result in nonstationary landing motions. This behavior has been predicted theoretically in Sec. II but can also be observed in the simulation results in Fig. 24. Note that, despite the associated conservatism of the results depicted in Fig. 6 with $\Theta_\tau = 0$ deg, the minimum wind speed that would lead to a reliable landing is the same as the minimum wind speed required for the nonassisted launching, which is $v_w = 8$ m/s. Theoretically, this would allow the kite to hover at constant tether length at every altitude during the landing procedure. Reeling in the tether increases the apparent wind speed and hence would only lead to higher tension and eventually to a higher elevation angle. Although the maximum tension in the tether has to be respected, the main boundary for the

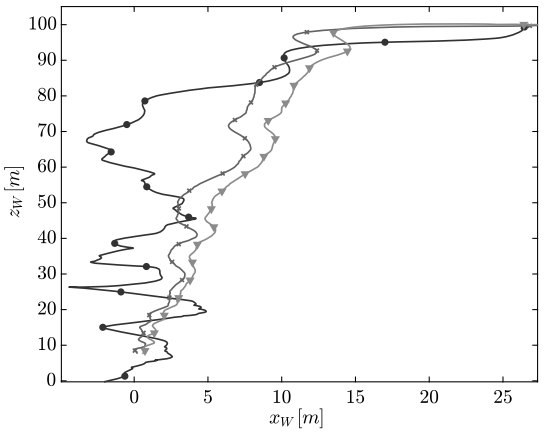

Fig. 21 Kite trajectories with $W_{20} = 4$ m/s (circles), 7 m/s (crosses), and 10 m/s (triangles).

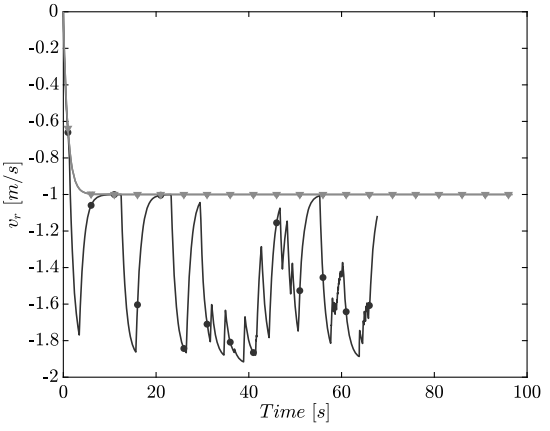

Fig. 22 Reeling-in speeds for $W_{20} = 4$ m/s (circles), 7 m/s (crosses), and 10 m/s (triangles).

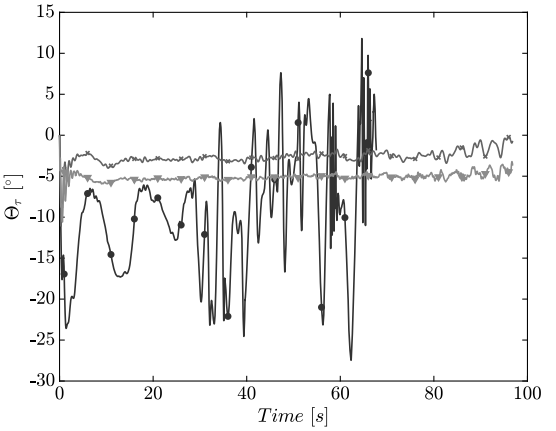

Fig. 23 Pitch angles for $W_{20} = 4$ m/s (circles), 7 m/s (crosses), and 10 m/s (triangles).

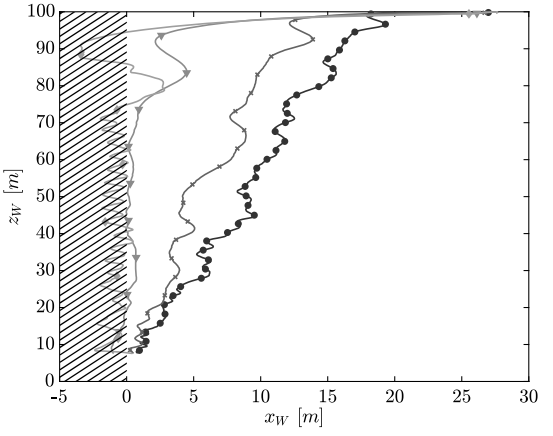

Fig. 24 Kite landing path with $\bar{v}_r = -0.5$ m/s (circles), −1 m/s (crosses), −2 m/s (triangles), and −3 m/s (diamonds).

reeling-in speed during landing is given by the maximum elevation angle $\phi = 90$ deg. Numerical simulations with $v_{20} = 8$ m/s and different nominal reeling-in velocities in combination with the force-feedback controller have been conducted to qualitatively demonstrate this effect, and the results are depicted in Fig. 24. Conservatively, for a wind speed of 8 m/s, a reeling-in speed until ≈ -1.6 m/s allows a steady descent of the kite, as can be deduced from Fig. 6. Using the less conservative results from Fig. 7, a reeling-in speed until -2 m/s can lead to a steady landing behavior. In this case, the equilibrium elevation angle would be $\phi \approx 90$ deg. These theoretical results match very well with the simulation results depicted in Fig. 24, where the almost vertical (i.e., $\phi \approx 90$ deg) trajectory indicated by the triangular markers is obtained with a reeling-in speed of $\bar{v}_r = -2$ m/s. Higher reeling-in speeds (e.g., $\bar{v}_r = -3$ m/s) lead to trajectories with $\phi > 90$ deg, as indicated by the diamond-shaped markers in Fig. 24.

From a methodological point of view, the nominal reeling-in speed $\bar{v}_r$ should be based on the measured reference wind speed W_{20}. Although higher wind speeds at the kite during the descend phase are expected, this will not violate the equilibrium conditions, as can be observed in Fig. 6. In fact, the boundaries for the wind speed W_{20} and reeling speed $\bar{v}_r$ should be determined based on Fig. 6, which are conservative bounds but guarantee a safe and predictable landing performance. This is due to the fact that, in both the launching and landing cases, the pitch angle Θ_t moves the minimum wind speeds to lower values. In future models, the pitch angle could be expressed in terms of the apparent wind speed, which will allow to calculate less conservative bounds, including a safety factor that can be chosen manually.

D. Summary of the Methodology

In this section, the presented simulation results are used to summarize the proposed VTOL methodology for flexible wing kite power systems. At this stage, the methodology relies on the following key assumptions: 1) knowledge of $C_L(\alpha)$ and $C_D(\alpha)$ curves of the kite as well as the geometric properties of the kite such as wing area, bridle length, and weight; 2) available wind speed measurement on the ground at 6 m; 3) availability of a shear wind model that maps altitude to wind speed; and 4) knowledge of the downwind direction.

If the previous requirements are satisfied, the kite can be launched and landed according to the following procedures. First, verify before the kite launch if, for the measured reference velocity W_{20}, a parking elevation angle ϕ exists using Fig. 5. In the following, it will be assumed that such an equilibrium exists, otherwise the kite cannot be launched using the presented methodology. Second, verify if $W_{20} > W_{20,\min} = 8$ m/s. If this condition is satisfied, the kite can be launched using the force-based winch controller without multicopter assistance. As soon as the kite reaches the operational altitude, the winch stops reeling out the tether, and the kite will be steered into the parking position, which terminates the launching phase. If $W_{20,\min} < 8$ m/s, the multicopter can be used to drag the kite to the operational altitude h_r. The operational altitude can be predicted using a shear wind field model as well as the minimum wind speed $v_W(h_r)$ that fulfills the parking equilibrium condition, here $v_W(h_r) = 8$ m/s. Note that usually release altitudes higher than 100 m are required from an operational point of view, which means that $h_{r,\min} = 100$ m. At the operational altitude, the kite will be released, and the reeling out of the tether will be stopped. The multicopter will continue following the landing path, while the kite stays in the parking position until the multicopter is landed. After the multicopter has landed, the power-production cycle is triggered.

For the landing, the following procedure is proposed. The landing will be conducted without the multicopter, and it is assumed that the kite is already in the parking position. First, the wind measurement on the ground will be used to check if $W_{20} > W_{20,\min} = 8$ m/s. If this condition is satisfied, the kite can be reeled in using the tether force-feedback controller. Note that if this condition is not satisfied, a controlled reeling in of the kite toward the mast is still possible, as can be observed in Fig. 21, where a controlled landing was possible until 6 m/s. However, the kite will descend in a less predictable and nonstationary manner, which will make it difficult to land the kite such that it can be relaunched without external assistance or even damage the kite on impact.

VI. Conclusions

In this paper, a vertical launching and landing methodology for flexible wing kite power systems was proposed and evaluated by means of simulations and an equilibrium analysis. The equilibrium analysis turned out to be an effective method to calculate boundary conditions that frame the launching and landing envelope. Results from the equilibrium analysis show that a more refined kite point-mass model that includes gravity and drag of the tether is necessary to obtain less conservative results. This conservatism has been confirmed by the simulation results and is a result of the negative pitch angle due to the weight and drag of the steering unit and tether. Furthermore, it can be concluded that, with the multicopter assistance, the launching envelope of the kite can be enlarged by reducing the minimal ground wind speed from 8 m/s down to at least 5 m/s. Moreover, using the proposed tether force-feedback winch controller, it could be demonstrated that, for ground wind speeds greater than 8 m/s, the kite can be launched and landed robustly without additional external assistance. Also, the simulation results demonstrate that the tangential motion of the kite is implicitly controlled through the aerodynamic damping, as expected from the equilibrium analysis. Hence, it is sufficient during launching and landing to control the radial motion either only by the winch or in case of low-wind-speed conditions by the winch and the multicopter path-following controller.

Acknowledgments

This research has been supported financially by the project Airborne Wind Energy System Modelling, Control and Optimisation (AWESCO) (H2020-ITN-642682), funded by the European Union's Horizon 2020 Research and Innovation Program under the Marie Sklodowska-Curie grant agreement 642682. The authors would like to thank the team of Kitepower BV for supporting this work, in particular Marcos Jerez Venegas for conducting a first preliminary small-scale experimental study.

References

[1] Ahrens, U., Diehl, M., and Schmehl, R. (eds.), *Airborne Wind Energy, Green Energy and Technology*, Springer, Berlin, 2013, pp. 111–113. doi:10.1007/978-3-642-39965-7

[2] Fagiano, L., and Schnez, S., "On the Take-Off of Airborne Wind Energy Systems Based on Rigid Wings," *Renewable Energy*, Vol. 107, July 2017, pp. 473–488. doi:10.1016/j.renene.2017.02.023

[3] Haug, S., "Design of a Kite Launch and Retrieval System for a Pumping High Altitude Wind Power Generator," M.S. Thesis, Univ. of Stuttgart, Stuttgart, Germany, 2012. doi:10.18419/opus-3936

[4] Cherubini, A., Papini, A., Vertechy, R., and Fontana, M., "Airborne Wind Energy Systems: A Review of the Technologies," *Renewable and Sustainable Energy Reviews*, Vol. 51, Nov. 2015, pp. 1461–1476. doi:10.1016/j.rser.2015.07.053

[5] Bauer, F., Hackl, C. M., Smedley, K., and Kennel, R., "On Multicopter-Based Launch and Retrieval Concepts for Lift Mode Operated Power Generating Kites," *Book of Abstracts of the International Airborne Wind Energy Conference 2015*, edited by R. Schmehl, Delft Univ. of Technology, Delft, The Netherlands, 2015, pp. 92–93. doi:10.4233/uuid:7df59b79-2c6b-4e30-bd58-8454f493bb09

[6] Fechner, U., van der Vlugt, R., Schreuder, E., and Schmehl, R., "Dynamic Model of a Pumping Kite Power System," *Renewable Energy*, Vol. 83, Nov. 2015, pp. 705–716. doi:10.1016/j.renene.2015.04.028

[7] Jehle, C., and Schmehl, R., "Applied Tracking Control for Kite Power Systems," *Journal of Guidance, Control, and Dynamics*, Vol. 37, No. 4, 2014, pp. 1211–1222. doi:10.2514/1.62380

[8] Valavanis, K. P., and Vachtsevanos, G. J. (eds.), *Handbook of Unmanned Aerial Vehicles*, Springer, Dordrecht, The Netherlands,

2014, pp. 243–277.
doi:10.1007/978-90-481-9707-1

[9] Stevens, B. L., Lewis, F. L., and Johnson, E. N., *Aircraft Control and Simulation*, Wiley, Hoboken, NJ, 2016, p. 1, 674.
doi:10.1002/9781119174882

[10] Bosch, A., Schmehl, R., Tiso, P., and Rixen, D., "Dynamic Nonlinear Aeroelastic Model of a Kite for Power Generation," *Journal of Guidance, Control, and Dynamics*, Vol. 37, No. 5, 2014, pp. 1426–1436.
doi:10.2514/1.G000545

[11] Falconi, G. P., Heise, C. D., and Holzapfel, F., "Fault-Tolerant Position Tracking of a Hexacopter Using an Extended State Observer," *Proceedings of the 6th International Conference on Automation, Robotics and Applications*, Inst. of Electrical and Electronics Engineers (IEEE), New York, Feb. 2015, pp. 550–556.
doi:10.1109/ICARA.2015.7081207

[12] Lavretsky, E., and Wise, K. A., *Robust and Adaptive Control*, Springer–Verlag, London, 2013, pp. 51–62.
doi:10.1007/978-1-4471-4396-3